Dynamics of the 1800 ^{14}C yr BP Caldera-Forming Eruption of Ksudach Volcano, Kamchatka, Russia

Benjamin J. Andrews[1], James E. Gardner[1], Steve Tait[2],
Vera Ponomareva[3], and Ivan V. Melekestsev[3]

The 1800 ^{14}C yr BP Ksudach KS_1 rhyodacite deposits present an opportunity to study the effects of caldera collapse on eruption dynamics and behavior. Stratigraphic relations indicate four Phases of eruption, Initial, Main, Lithic, and Gray. Well-sorted, reverse-graded pumice fall deposits overlying a silty ash compose the Initial Phase layers. The Main, Lithic, and Gray Phases are represented by pumice fall layers interbedded with pyroclastic flow and surge deposits (proximally) and co-ignimbrite ashes (distally). Although most of the deposit is <30 wt.% lithics, the Lithic Phase layers are >50 wt.% lithics. White and gray pumice are compositionally indistinguishable, however vesicle textures and microlite populations indicate faster ascent by the white pumice prior to eruption of the Gray Phase. The eruption volume is estimated as ~8.5 km^3 magma (dense rock equivalent) and ~3.6 km^3 lithics. Isopleth maps indicate mass flux ranged from 5–10x10^7 kg/s during the Initial Phase to >10^8 kg/s during the Main, Lithic, and Gray Phases. Caldera Collapse during the Lithic Phase is reflected by a large increase in lithic particles and the abrupt textural change from white to gray pumice; collapse began following eruption of ~66% of the magma, and finished when ~72% of the magma was erupted. Stratigraphic, granulometric, and component analyses indicate simultaneous eruption of buoyant plumes and non-buoyant flows during the Main, Lithic, and Gray Phases. Although mass flux did not change significantly following caldera collapse, the Gray Phase of eruption was dominated by non-buoyant flows in contrast to the earlier Phases that erupted mostly buoyant plumes.

1. INTRODUCTION

Understanding the effects of caldera collapse on explosive eruption dynamics constitutes a fundamental question in volcanology. Caldera collapse may significantly alter the vent structure and, as a result, may change the eruption behavior (Dobran et al., 1993). Of particular interest are changes in mass flux, magma ascent rate, the potential for transitions of eruption regime from buoyant, Plinian behavior to dominantly pyroclastic flow generation), and the timescales over which these changes occur. The most recent caldera-forming eruption of Ksudach volcano (Figure 1) provides an opportunity to examine these processes in detail because distinct eruption phases can be recognized in the deposits and most of the tephra was deposited from a buoyant, Plinian column (Braitseva et al., 1996), allowing for an estimation of variations in mass flux throughout the eruption.

[1] Department of Geology and Geophysics, Jackson School of Geosciences, The University of Texas at Austin, Austin Texas

[2] Laboratoire de Dynamique des Systemes Geologiques, Institut de Physique du Globe, Paris, France

[3] Institute of Volcanology and Seismology, Petropavlovsk-Kamchatsky, Russia

325
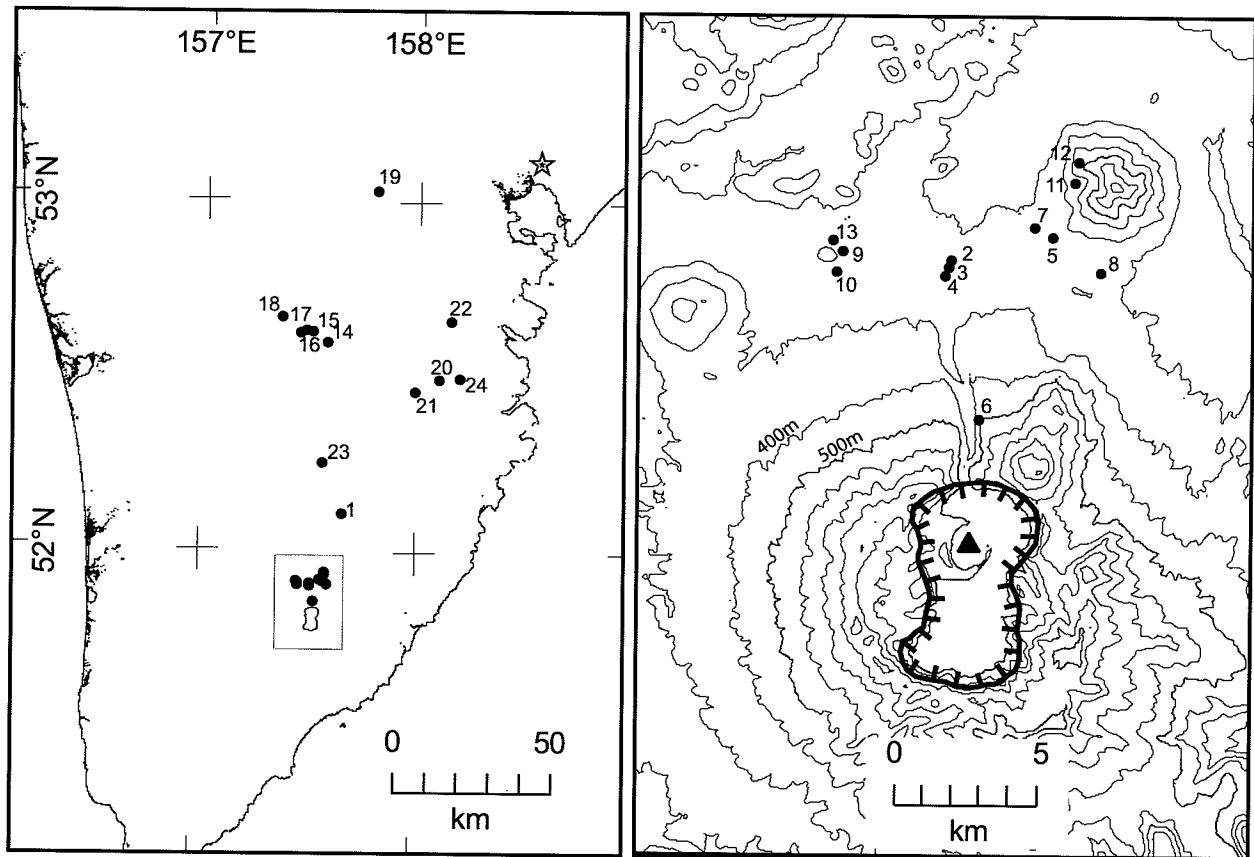
Figure 1. Location of Ksudach and sample locations. Locations of Petropavlosk-Kamchatsky and Stübel Cone' Volcano are indicated by the star and triangle, respectively. Contour interval in insert is 100 m.

The KS_1 eruption occurred in 1800 ^{14}C yr BP forming the ~4x6.5 km Caldera V when 8–9 km3 (DRE) of rhyo-dacite magma erupted (Braitseva et al., 1996; Volynets et al., 1999; this study). The KS_1 eruption initiated with phreatomagmatic activity but quickly changed to magmatic fall and pyroclastic flow eruption (Braitseva et al., 1996). Column heights ranged from 22 to 30 km during the eruption (Bursik et al, 1993; Braitseva et al., 1996). During the course of the eruption, the dispersal axis of the eruption plumes rotated from a north-northeast to more northerly direction, while the pumice color changed abruptly from white to gray. Bulk compositions of the two pumice types are identical, suggesting that the color difference results from different sizes and distributions of Fe-oxide microlites (Volynets et al., 1999).

In this paper we build on the earlier works with the aim of providing more detailed data on the evolution of the dynamics of the KS_1 eruption. One specific objective was to look for evidence in the deposits for the onset of caldera collapse and how this may have affected the dynamics. The total KS_1 deposit volume, mass fluxes throughout the

eruption, and the timing of caldera collapse have been constrained through stratigraphic and component analyses. Relative magma ascent rates and changes in conduit geometry have been derived through analysis of vesicle textures and microlite number densities in pumice in conjunction with estimates of discharge rate.

2. METHODS

2.1 Field Studies

Stratigraphic sections were logged at 24 locations (Figure 1). At every location, the thickness of each tephra layer present was measured. The five largest lithic clasts were sampled from the excavated volumes of most pyroclastic fall layers and the long and short axes of each were measured. Samples analyzed for grain-size distribution and componentry were collected immediately after stratigraphic observations, and their stratigraphic locations are noted in Table 1. All samples were collected as bulk samples large enough to be representative of the layer

from which they were taken; thus bulk sample weights range from ~0.1 to 2 kg. Care was taken to sample only portions of a layer that could be considered "massive." In instances where a layer was graded, samples were collected either from the base and top, or their location within the layer was noted.

2.2 Granulometric and Component Studies

Samples were wet sieved in 0.5ϕ size fractions from the coarsest particles to 4.0ϕ (ϕ = -log$_2$[diameter in mm]). Mass fractions of each size were determined from the dry weights. After drying and weighing, sizes of the fractions finer than 4ϕ were measured using a Spectrex Laser Grain Size Analyzer to 7ϕ. Several fall samples were too coarse to fully retrieve from the field and were dry sieved in the field in 1ϕ intervals down to -2ϕ; the finer fraction was then wet sieved in the laboratory. Componentry of the coarse fractions of those field samples was determined prior to discarding, using "pumice" and "lithic" as designators.

Granulometric and component analyses (Table 1) were combined with field observations of depositional structures and stratigraphic facies to distinguish layers as fall, flow, or surge deposits, following the criteria of Walker (1981). Pumice and ash fall layers are described by a high degree of sorting (σ_ϕ < 2.0ϕ) and a unimodal grain-size distribution. Layers with polymodal grain-size distributions frequently occur; in general, the coarser modes of these deposits are well-sorted. Pyroclastic flow deposits are characterized by poorer sorting, whereas surge deposits are finer grained, moderately sorted, and commonly have internal structures. Well-sorted layers relatively enriched in fine-grained material are termed co-ignimbrite ashes (Md_{50} < 4ϕ).

Component mass fractions have been analyzed for 39 samples (Figure 1, Table 1). Random splits of 500 particles were taken from each size fraction 2ϕ and coarser and counted with the aid of a binocular stereo zoom microscope (up to 40x) and 10x hand lens. Weight fractions were calculated from modal fractions by determining average weights for each particle type in each size fraction: 100 pumice and 100 lithics were separated from each 0.5ϕ size fraction between -2ϕ and 2ϕ, crystals were separated at -1ϕ and 1.5ϕ; average weights for each component in a particular size fraction were measured, or interpolated from a best fit equation for those size fractions not measured directly. For size fractions with fewer than 500 particles, all particles were counted, and for those fractions with fewer than 100 particles, the individual component masses weighed.

Component types were determined observationally during fieldwork, sieving, and component analysis. The types of particles observed are pumice (white or gray),

crystal, poorly-vesicular juvenile (obsidian) clasts, gray lithic, altered lithic, and granitoid. Pumice, the most common component of nearly all samples, is typically equant, although some white pumice, particularly in the smaller (<1ϕ) size fractions, are highly elongated. Crystals, often with adhering glass, and occasionally clotting together, are almost entirely plagioclase and pyroxene; magnetite and ilmenite may occur as discrete crystals but are generally indistinguishable from small black juvenile clasts. Juvenile, non-vesicular volcanic particles are generally black, glassy, roughly equant, and have <10 vol.% vesicles. Gray lithics are non-altered lava and porphyritic rocks. Some altered volcanic lithics are present, and are distinguished by their weathered and/or oxidized appearance. Pieces of granitoid rocks and occasional cumulates are differentiated from crystal clots by a generally finer grain-size, closer packing, and more equant particle shape. Feldspars and pyroxenes appear to be the dominant phases within granitoid particles.

2.3 Textural Analysis of White and Gray Pumice

White and gray pumice lapilli from stratigraphic site KSU-23 were selected for bulk vesicularity measurements, and back-scattered electron imaging and image analysis during component analysis. Groups of 5 pumice from the 0ϕ size fraction were selected and analyzed for average bulk density, using the methods of Gardner et al. (1996). Bulk vesicularities were calculated from the bulk density by assuming a non-vesicular density of 2500 kg/m^3.

Polished thin sections were made of 10 pumice from KSU-23H and KSU-23b, separated from the 0ϕ size fractions of each sample. Reflected and transmitted light images were taken of the pumice. The slides were then carbon coated and imaged using back-scattered electron (BSE) imaging. The resulting high contrast images were converted to binary images using Scion Image®, and vesicularities of individual pumice and portions of pumice analyzed. Long and short dimensions of vesicles were measured in each image and used to calculate bubble size and aspect ratio. Coalescing vesicles were treated as their multiple, constituent vesicles during measurement. Plagioclase and oxide volumetric microlite number densities, N_v, were calculated from these images using the expression:

$$N_v = \left(\frac{N}{A}\right)^{3/2}$$

where N is the number of microlites counted in an area A of an image (derived from Hammer et al., 1999).

Table 1. Granulometric data for KS$_{-1}$ samples. Graphic mean and standard deviation, M_z and σ_g, are presented in units of ϕ. Sample componentry data are presented as wt% of each component. See Figure 1 for sample locations.

| Sample	Phase	Type	M_z	σ_g	pumice	crystal	glass	alt.-lith.	lithic	granitoid
KSU-01A	Init.	fall	3.17	2.01	73.8	6.0	10.7	0.1	9.2	0.2
KSU-01B	Init.	fall	-0.01	1.82	66.1	10.1	3.8	0.9	18.8	0.3
KSU-01C	Init.	fall	0.35	1.88	45.7	6.8	1.5	1.8	43.9	0.4
KSU-01D	Main	flow	-1.57	2.05	63.3	1.9	1.3	2.7	29.1	0.3
KSU-01F	Main	fall	.69	3.25	70.6	1.5	0.9	1.2	25.6	0.2
KSU-01G	Main	fall	-0.73	0.75	23.0	8.3	13.3	7.0	47.7	0.8
KSU-01H	Lith.	fall	-0.65	0.68	28.6	8.2	1.6	3.4	56.9	0.7
KSU-01I	Lith.	fall	-1.56	1.69	88.8	2.6	˙7.2	2.5	29.7	0.3
KSU-01J	Lith.	fall	-0.72	0.98	6.9	1.8	0.9	0.4	89.6	0.4
KSU-09F	Gray	fall	-0.20	2.49						
KSU-10A	Init.	fall	3.99	1.68						
KSU-10B	Init.	fall	-0.76	2.11						
KSU-10D	Main	fall	1.79	2.56						
KSU-10F	Main	fall	-2.48	2.45						
KSU-10H	Lith.	fall	-0.45	2.47						
KSU-10I	Lith.	fall	-1.58	2.71						
KSU-10J	Lith.	fall	-2.38	1.62						
KSU-12A	Init.	fall	-2.30	1.93	55.0	1.5	1.3	1.2	40.2	0.8
KSU-12B	Init.	fall	-2.55	2.06	69.1	1.0	0.9	2.22	6.1	0.7
KSU-12D	Main	fall	-3.19	1.65	65.3	1.0	3.9	2.1	26.5	1.3
KSU-12E	Main	fall	-1.58	2.68	41.4	2.6	5.2	1.1	48.5	1.2
KSU-12F	Gray	fall	2.75	2.92	73.7	1.5	5.7	0.0	18.8	0.2
KSU-12G	Gray	fall	-3.37	2.04	81.9	1.1	1.2	4.9	10.2	0.8
KSU-14A	Gray	fall	2.66	1.82	60.8	3.9	4.4	0.0	30.9	0.0
KSU-14B	Gray	fall	1.60	2.54	68.8	2.4	5.0	0.0	24.1	0.0
KSU-14C	Gray	fall	-0.23	1.76	68.9	4.6	3.8	0.0	22.9	0.2
KSU-14D	Gray	fall	1.46	1.91	51.4	6.8	2.5	0.0	38.9	0.3
KSU-14E	Lith.	fall	1.22	0.86	34.5	12.3	2.3	0.3	50.3	0.3
KSU-14F	Main	fall	0.69	1.38	56.5	8.7	1.8	0.1	32.7	0.3
KSU-14G	Main	fall	0.48	1.29	54.1	12.3	2.2	0.1	31.0	0.2
KSU-14H	Main	fall	0.49	1.23	56.8	12.6	0.8	0.0	29.8	0.1
KSU-14I	Main	fall	3.27	2.11	79.9	5.3	1.2	0.0	13.6	0.1
KSU-19A	Gray	fall	1.32	0.76						
KSU-23A	Gray	fall	-1.70	1.67	71.8	2.7	18.3	1.2	5.1	0.0
KSU-23C	Lith.	fall	0.06	1.07	14.1	3.7	16.5	0.0	64.6	1.1
KSU-23D	Lith.	fall	-0.73	1.47	33.3	3.8	17.4	0.2	41.6	2.1
KSU-23F	Lith.	fall	-0.42	1.53	38.3	8.9	14.8	5.4	27.1	4.1
KSU-23H	Main	fall	-1.62	1.58	74.5	2.8	8.2	2.8	10.8	0.3
KSU-23I	Main	fall	-1.05	1.59	66.9	6.0	7.5	3.9	13.7	1.4
KSU-23L	Init.	fall	1.91	2.34	80.5	6.6	4.2	0.7	6.9	1.0
KSU-01E	Main	flow	1.12	3.14	87.3	2.2	3.1	1.1	6.2	0.0
KSU-09C	Main	flow	5.16	1.43						
KSU-10C	Main	flow	3.71	2.16						
KSU-10G	Main	flow	4.44	2.30						
KSU-10K	Gray	flow	-0.12	2.10						
KSU-10L	Gray	flow	-0.08	1.94						
KSU-12C	White	flow	4.88	1.43	97.1	0.4	0.5	0.1	1.8	0.1
KSU-12I	Gray	flow	-0.03	3.04	75.6	3.7	7.2	0.7	12.3	0.3
KSU-21D	Main	flow	-0.58	1.17						
KSU-21E	Main	flow	3.88	2.78						
KSU-21F	Init.	flow	0.12	1.00						
KSU-23B	Gray	flow	1.94	2.87	40.7	3.0	3.0	0.3	53.0	0.1
KSU-23E	Lith.	flow	1.63	2.76	53.9	6.3	0.6	0.1	39.4	0.1
KSU-23G	White	flow	1.80	2.65	48.7	8.2	1.9	0.6	40.5	0.1
KSU-23J	White	flow	3.42	2.53	72.7	4.7	2.4	0.3	19.9	0.1
KSU-23K	White	flow	1.91	2.57	79.0	6.5	5.3	0.1	8.4	0.5

3. RESULTS

3.1 Tephra Stratigraphy and Granulometric and Component Analysis

The KS_1 deposit decreases in thickness and complexity with distance (Figure 2), from >20 m at 4 km from the caldera, to approximately 10 cm at 100 km. The abrupt change from white to gray pumice that is ubiquitous in the upper portion of the sequence provides a distinct time horizon in the deposits. Proximal deposits are composed of numerous flow, surge, and fall layers. In general, the number of correlative fall deposits increases with distance, and the fraction of total deposit composed of fall layers increases from ~30% to 100% within 25 km from the caldera. Ash fall layers occupy similar stratigraphic positions in medial and distal locations as do flow and surge layers in proximal locations.

The decrease in stratigraphic complexity with distance is particularly apparent when across-axis variations in proximal and distal deposits are compared. In proximal areas,

correlation of individual layers is difficult (Figure 3a). Flow deposits several meters thick at one section may be absent only a few kilometers away, and erosion by pyroclastic density currents may or may not have removed underlying fall and flow deposits. This is in marked contrast to distal deposits, where fall layers are highly correlative across many tens of kilometers (Figure 3b).

The color change, stratigraphic relations, and componentry have been used to group layers into four distinct eruptive phases of the deposit. These phases are an Initial Phase of mainly reversely-graded fall deposition; a Main Phase of fall and flow deposition; a Lithic-rich Phase dominated by fall deposition; and a Gray Phase of fall and flow deposition (Figure 2, section KSU-01). It should be noted that the interbedded proximal fall and flow layers and medial and distal fall and ash layers are not graded. That is, individual fall layers of a particular phase have relatively constant modes at individual sites despite the occurrence of interbedded fine-grained layers. Isopachs and isopleths were mapped for the pumice fall and ash fall layers of each eruption phase, all of which are strongly elongate to the north-northeast. Those
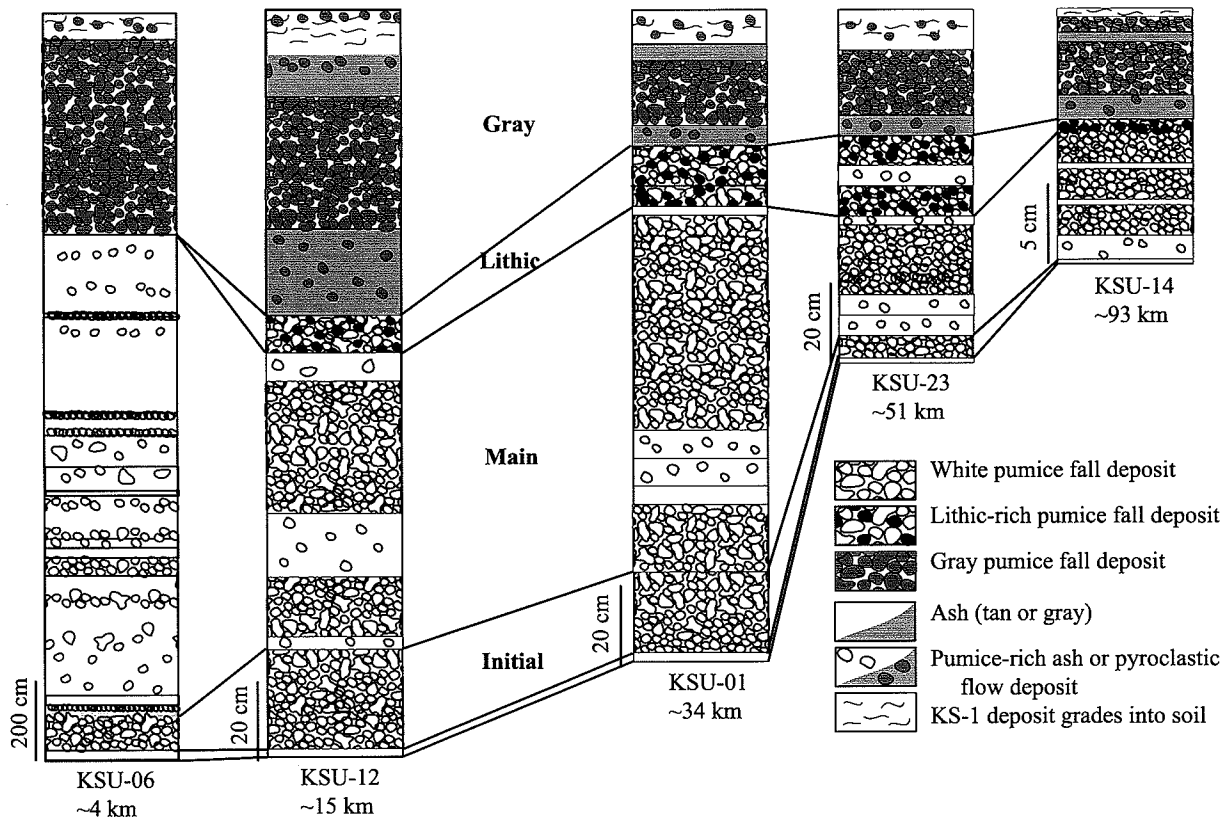
Figure 2. Fence diagram illustrating variations in stratigraphy with distance from the caldera. The complexity of the deposits decreases significantly with distance from the volcano. This is particularly true with regard to interbedding of pumice falls with pyoclastic flows and/or coignimbrite ashes. See Figure 1 for sample locations.
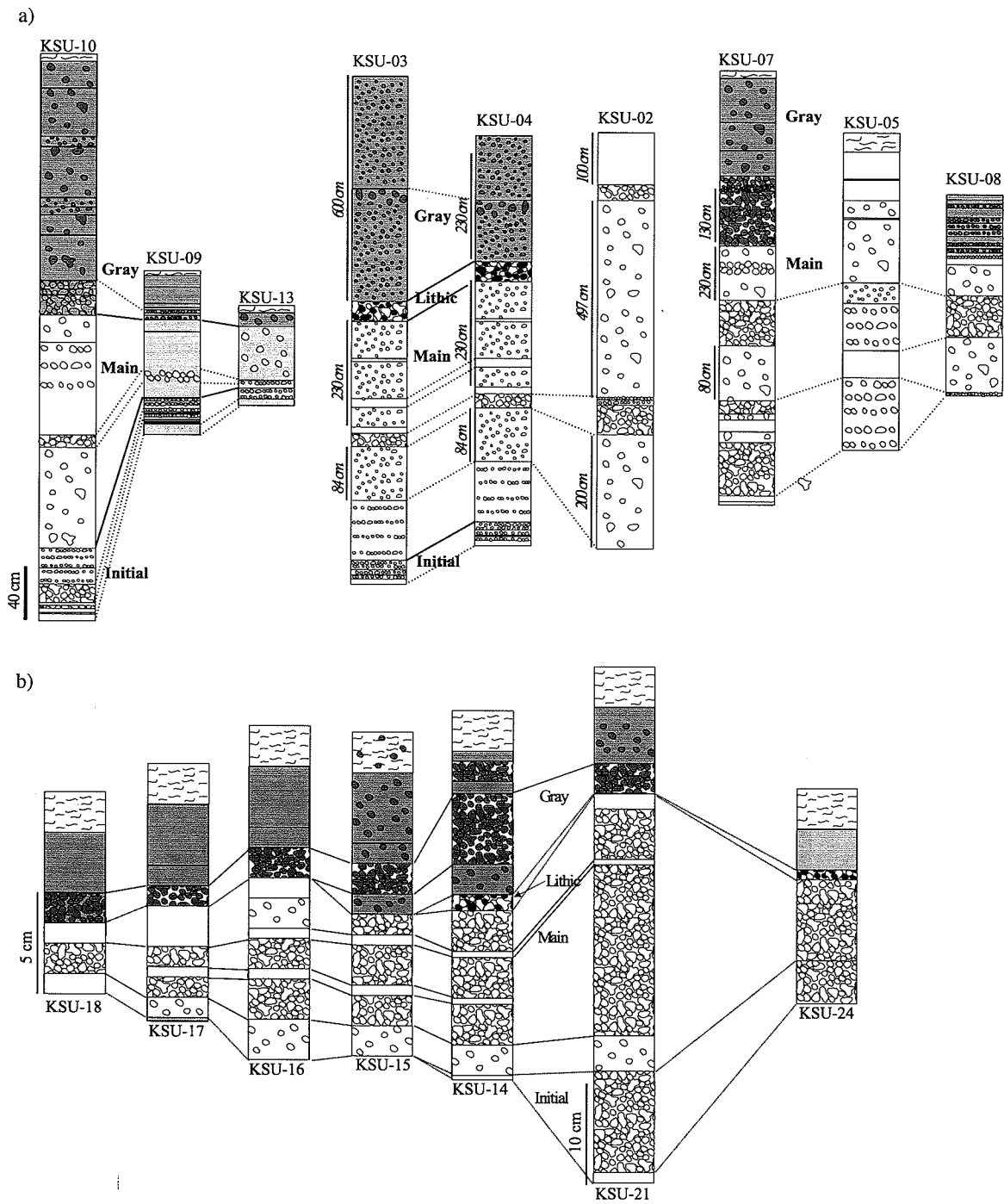
Figure 3. a.) Fence diagrams illustrating variations in proximal deposits. Individual layers do not necessarily correlate well between proximal deposits. Deposit thicknesses can vary substantially over relatively short distances. Pumice fall layers may be present at one location, but completely absent a few hundred meters away (e.g. sites KSU-07, KSU-08, and KSU-05). Locations of fences are shown in Figure 1; stratigraphic legend is shown in Figure 2. **b.)** Fence diagram illustrating across-axis variation in distal stratigraphy. The stratigraphic complexity apparent in proximal deposits (Figure 3a) is largely missing in more distal sections. Pumice fall layers dominate the deposits prior to the white to gray change in pumice color. Gray Phase deposits are represented almost universally by pumice fall layers overlain by ash. See Figure 1 and 2 for sample locations and stratigraphic legend.

a)

b)
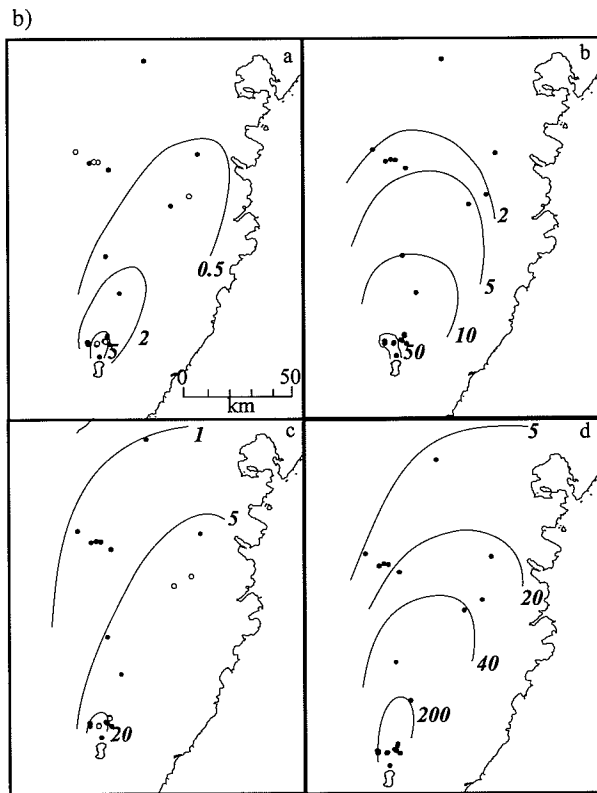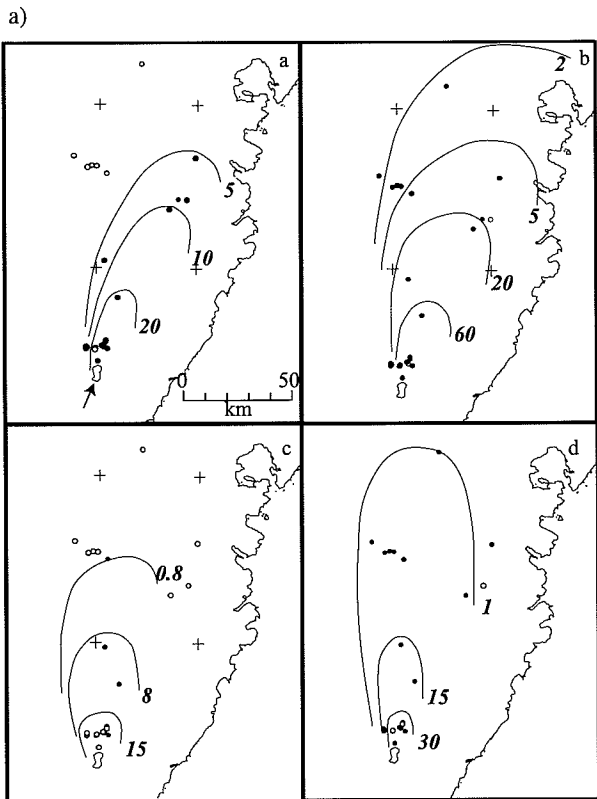
isopachs indicate that the depositional axis rotated ~30° to a more northerly direction during the eruption, in agreement with Bursik et al. (1993), and Braitseva et al. (1996) (Figures 4 and 5).

Volumes for the pumice fall layers were calculated from each isopach map, following the methods of Pyle (1989) and Fierstein and Nathenson (1992). In addition, co-ignimbrite ash volumes were calculated from isopachs of ash and pumice-bearing ash layers. Pyroclastic flow volumes were not directly calculated in this study, but are estimated at 3–4 km^3 of tephra by Braitseva et al. (Table 2). We estimate the total KS$_1$ deposit

Figure 4a. Pumice fall isopach maps. These maps represent the sum of pumice fall deposits at a particular site for a) Initial, b) Main, c) Lithic, and d) Gray eruption phases. Note that the depositional axis is elongate to the northeast of Ksudach, and rotated to a more northerly position as the eruption progressed. Contour value is in cm and indicated by the bold numbers. The location of Ksudach is indicated by arrow. Sample sites where the isopached eruption phase was not found are indicated by hollow circles.

Figure 4b. Isopach maps of cumulative fine-grained ash fall deposits for a) Initial, b) Main, and c) Gray eruption phases and d) total KS$_1$ deposit thickness. Contour interval is in cm.
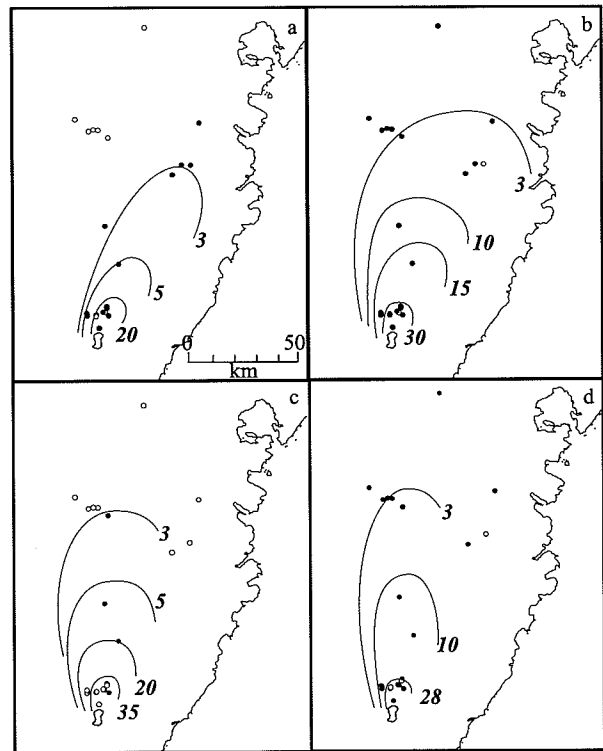
Figure 5. Pumice fall isopleth maps for a) Initial, b) Main, c) Lithic, and d) Gray eruption phases. Isopleth shapes indicate column height was greatest during the Main and Lithic Phases, slightly less during the Gray Phase, and lowest during the Initial Phase. Contour interval is in mm.

volume to be 20–25 km³ (8–9 km³ DRE) slightly larger than the 18–19 km³ (8 km³ DRE) calculated by Volynets et al. (1999) (Table 2). This estimate incorporates the pyroclastic flow deposit volume of 3–4 km³ estimated by Braitseva et al. (1996). All deposit volumes are converted to magma dense-rock equivalent (DRE) and lithic volumes, by subtracting the lithic fraction from the deposits and assuming a bulk juvenile deposit density of 1100 kg/m³ (Paladio-Melosantos et al., 1996) and magma density of 2500 kg/m³.

3.1.1 Initial Phase. Proximally, the Initial phase of deposition is defined by a reversely-graded, well-sorted, unimodal fall deposit, overlying poorly to moderately sorted silty ash layers (Figure 6). Braitseva et al. (1996) suggest that the lower ash layers were produced by phreatomagmatic explosions. The Initial Phase deposits contain ~70 wt.% pumice, with lithics and juvenile poorly-vesicular particles present in equal amounts (~10 wt.% each), and ~6 wt.% crystals (Figure 6). In proximal sections, the Initial Phase deposits are thicker
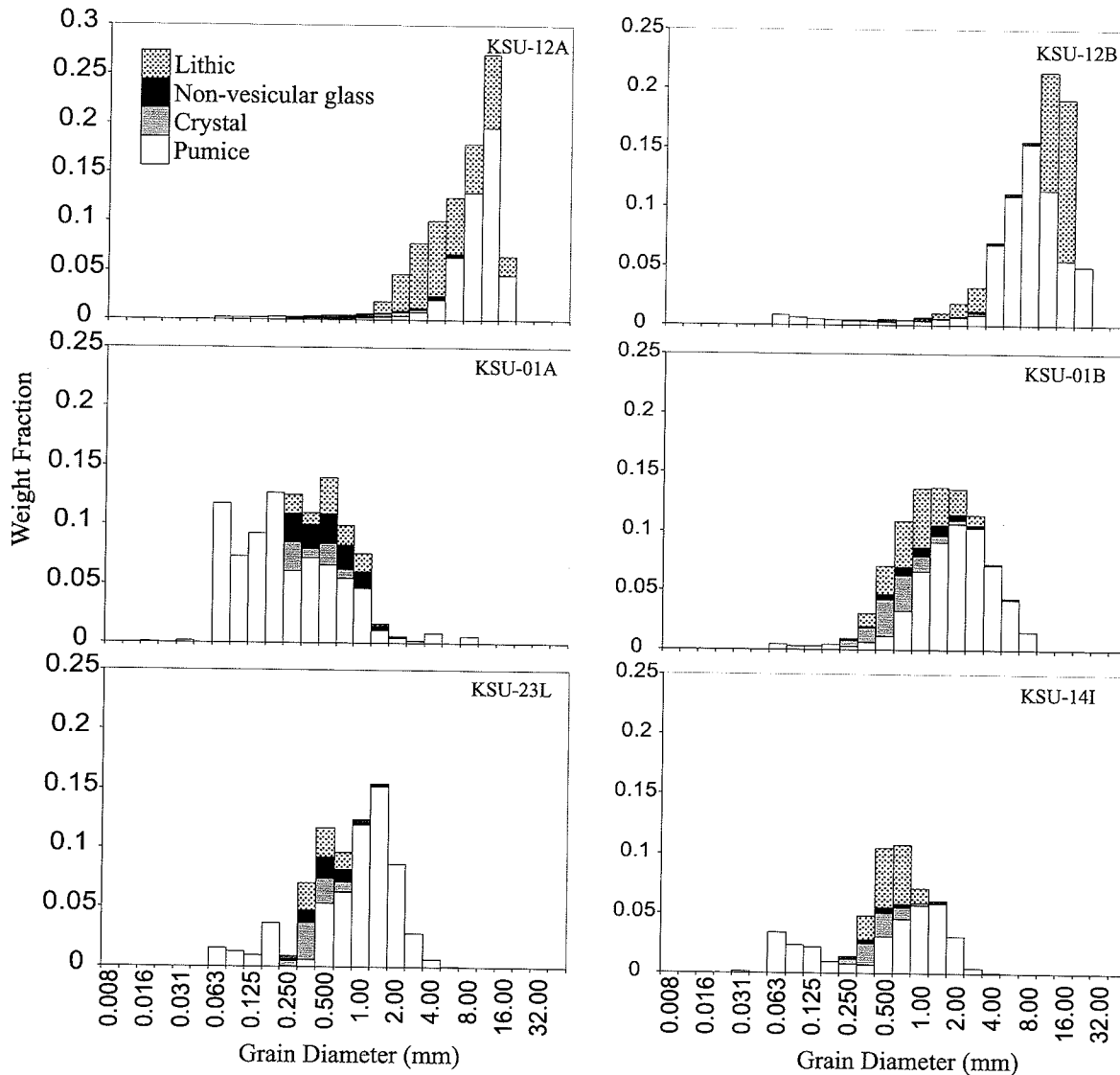
Figure 6. Initial Phase grain size plots. Stratigraphic height increases from left to right. Samples KSU-12A and KSU-12B exhibit prominent fin-grained tails and are skewed toward coarser grain sizes. The lowest sample from KSU-01, A, shows no sorting, however, the overlying Initial fall, B, displays excellent sorting, albeit with a fine-grained tail. The pumice bearing ashes from sites KSU-23 and KSU-14 both show distinct bimodal distributions. In general, the denser particles (i.e. not pumice) are well-sorted—this is particularly evident in samples KSU-12A, -01B, and -23L. Sample locations are shown in Figure 1.

Table 2. Eruptive volume calculated using the method of Pyle (1989) and Fierstein and Nathenson (1992). Volumes are displayed for pumice fall layers from the four eruptive phases, pyroclastic flow and ash layers from all phases except the Lith.ic phase. Total eruptive volume as calculated from the total deposit thicknesses and compared with sumn of individual volume layers. The number of isopachs, N, and 1- or 2-line approximation are noted.

Phase	Type	N	1- or 2-line	Volume (km³)
Initial	Pumice fall	3	1	3.3
	Flow/ash	3	2	0.4
Main	Pumice fall	4	2	9.8
	Flow/ash	3	2	4.3
Lithic	Pumice fall	3	1	1.4
Gray	Pumice fall	3	1	2.1
	Flow/ash	3	2	4.1
Total	Complete deposit	4	2	20.2
	Sum of individual layers			25.5

than 1 m, and multiple ash layers are frequently interbedded within the pumice fall layer (Figure 3b). The mode of fall layers increases in diameter upward through the deposits by as much as a factor of 4 (Figure 6). Distally, the Initial Phase is represented by a single coarse, bimodal ash fall layer (Figure 3a). The thickness of the Initial Phase deposits decreases to <5 cm ~100 km from the caldera. Down-axis, the coarse mode decreases in size from 8 to 0.7 mm and the deposit becomes richer in pumice and poorer in crystals.

3.1.2 Main Phase. The Main Phase of the KS_1 deposit is composed of interbedded fall and flow layers at proximal locations, pumice and ash fall layers at medial sites, and coarse and fine-grained ash fall layers at distal sites. The total thickness deposits decreases from >12 m at ~4 km from the caldera to less than 7 cm at ~100 km from the caldera (Figure 2). Main Phase fall layers are frequently bimodal or fines-enriched (Figure 7). Pumice accounts for 63–75 wt % of most Main Phase fall layers, but for greater than 85 wt.% of the coarsest medial layers (KSU-01G and H).

Pyroclastic flow and surge deposits frequently compose up to 90% of proximal Main Phase deposits. The contacts between many proximal fall layers and pyroclastic flow layers are often uneven, so that the thicknesses of fall layers pinch and swell as much as 1 m over length scales of ~10–100 meters. Pyroclastic flow deposits often contain lenses of rounded pumice. Flow deposits do not appear to form large, laterally continuous sheets, but rather numerous lobes complexly interbedded with fall deposits and each other (Figure 3b). Cross-stratified and laminated surge deposits are also present, particularly on topographic highs. Proximal, coarse fall layers overlying fine-grained ash layers show prominent fine-grained tails or secondary modes.

In medial and distal deposits, the Main Phase is dominated by pumice fall layers in which pumice are occasionally ash-coated (Figure 2). Ash fall layers compose up to 30% of the total Main phase thickness in medial and distal deposits; ash layers closer than ~60 km to the caldera are often pumice-bearing, whereas those in distal areas are generally free of coarse pumice. Medial and distal falls are relatively enriched in material <0.063 mm.

3.1.3 Lithic Phase. The Lithic Phase of the KS_1 deposit consists of one to several fall layers that contain 40–70 wt.% lithics. That constrasts with the <30 wt.% lithics in fall layers of other phases at the same locations (Figure 8). Lithic Phase layers are often missing at proximal localities, but are very distinctive at medial and distal sites, where they occur immediately below the white-to-gray change in pumice color. Pumice in the Lithic Phase is however always white. Two distinct fall layers separated by a centimeter-thick ash layer are observed at medial localities, but merge into one with distance. The total Lithic Phase thickness ranges from ~20 cm at 35 km from the caldera, to ~1 cm at 100 km from the caldera.

The Lithic Phase fall deposits are well sorted with fine-skewed grain size distributions. The pumice:crystal ratios (5–10:1) in those layers are very similar to those in fall layers of the other phases. In contrast, the lithic:crystal proportions of the Lithic Phase layers are substantially higher than in other layers (up to 15:1 versus ~2:1). These relationships indicate the componentry of the Lithic phase layers results from a 300–400% increase in lithic material rather than removal of pumice.

3.1.4 Gray Phase. Interbedded fall, flow, and ash deposits compose the Gray Phase KS_1 deposits, defined by having gray pumice in the deposit. Near the caldera, the pumice fall deposits are up to 5 m thick and are overlain by flow deposits <1 m thick (Figures 2 and 3b). At a distance of 15 km, the Gray Phase consists of 20-cm-thick pyroclastic-flow deposits overlain by a 30-cm-thick fall deposit, which is in turn overlain by a 25-cm-thick stratified pyroclastic-flow deposit. With distance those layers grade into pumice-bearing ash beds overlain by pumice fall deposits. Distally, a second, thin gray fall is observed near the top of the sections. Gray Phase deposits are ~6 cm thick in sections ~100 km from the caldera.

Pumice composes 65–80 wt% of Gray Phase deposits. The pumice fall deposits are typically well-sorted, but have minor secondary modes of very fine-grained ash (Figure 9). Lithics comprise 10–20 wt.%, similar to fall layers before the lithic phase, and crystals and non-vesicular juvenile particles are generally present in concentrations less than
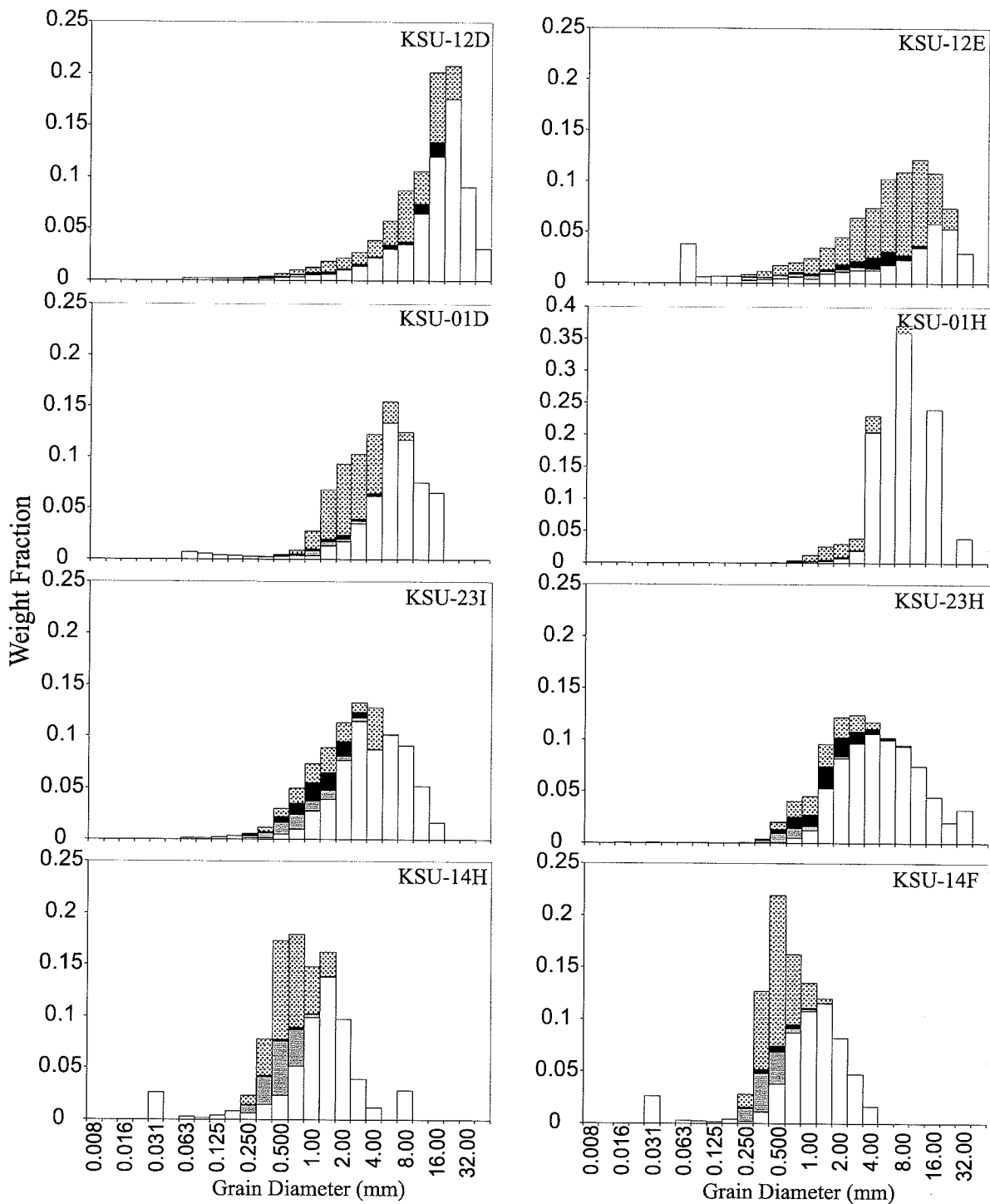
Figure 7. Grain size distributions and componentry of Main Phase fall deposits. Many Main Phase fall deposits are enriched in fine grained material; this is most apparent in samples from proximal locations such as KSU-12, but even well sorted fall deposits (e.g. KSU-23I) have minor fine-grained modes. The distal deposits, KSU-14H and -14F, display bimodal and fine skewed distributions, however, componentry data indicate that these distributions are the products of well-sorted pumice and dense particle distributions. See Figures 1 and 6 for samples locations and component legend.

Table 3. Pumice vesicularities as measured optically and with pycnometer for samples KSU-23H (white) and KSU-23A (Gray). The number of samples averaged for each measurement, N. Vesicularity is given as volume percent. Standard deviation of measurements is noted in italics.

Sample	Method	N	Ves (%)
KSU-23H	pyconmeter	15	78.2(*3.8*)
	optically	21	78.6(*4.3*)
KSU-23A	pycnometer	5	75.2(*3.3*)
	optically	17	75.1(*3.5*)

5 wt.%. The lowest gray ash layer in distal areas, however, has 40 wt.% lithics.

Stratigraphically, pyroclastic flow layers in proximal sections correlate with medial and distal bimodal pumice-bearing ash layers. Component analyses indicate the fine modes comprise well-sorted distributions of dense particles (primarily lithics and crystals). Proximal and medial pyroclastic flow and ash layers have componentry similar to the fall layers.

3.2 Textural Analysis

Bulk vesicularities of white and gray pumice are generally in the range of 75–80 vol% (Table 3). On average, white pumice are slightly more vesicular than gray pumice, but their ranges overlap. Despite their similar vesicularities, the shapes of vesicles in white and gray pumice are distinctly different (Table 4). White pumice contains vesicles that are typically 2–3 times more voluminous than those contained in gray pumice. Number densities of gray vesicles, $4–8 \times 10^4/mm^3$, are ~4 times greater than those in white pumice, $1–2 \times 10^4/mm^3$. Vesicles in white pumice generally have greater average aspect ratios (3:1 versus 2:1) than
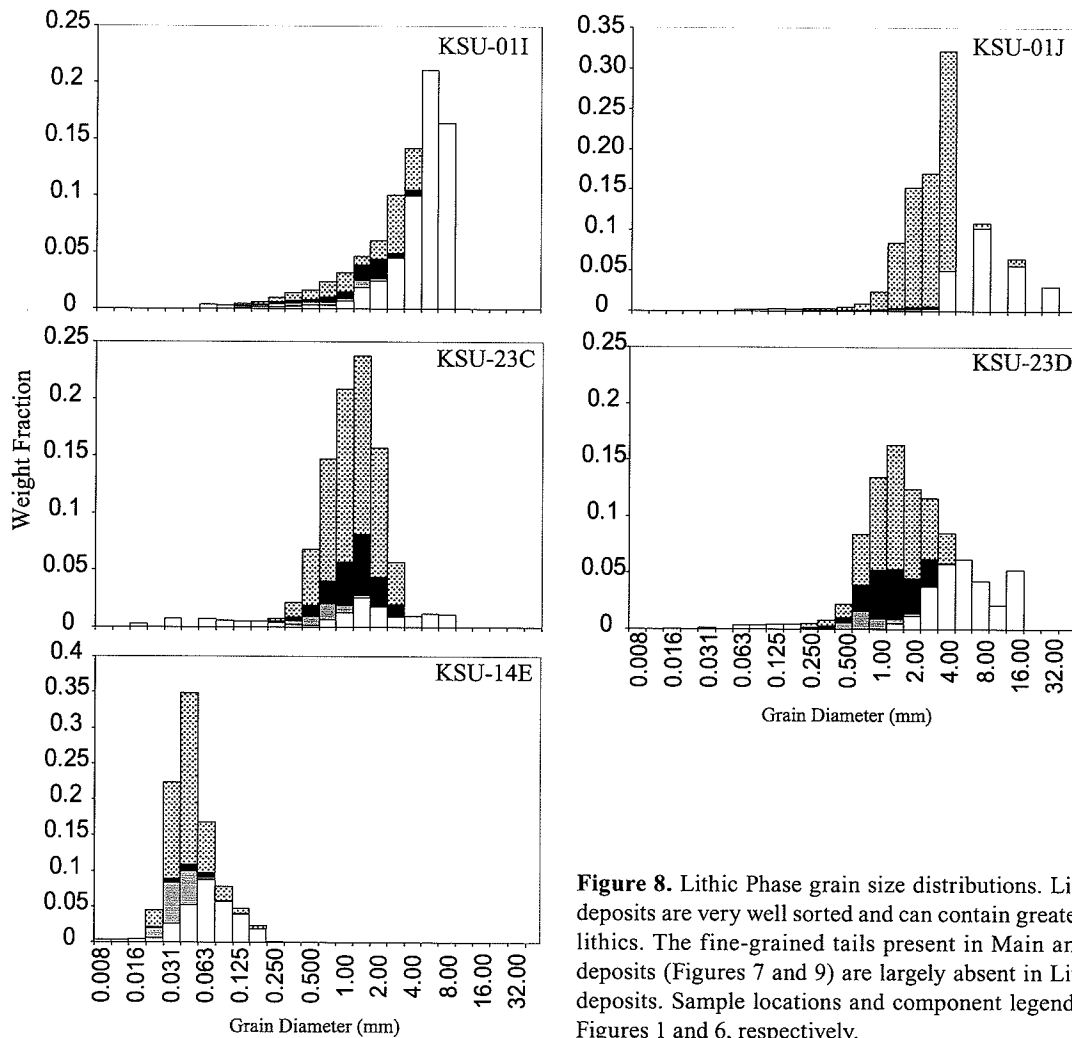
Figure 8. Lithic Phase grain size distributions. Lithic Phase fall deposits are very well sorted and can contain greater than 70 wt% lithics. The fine-grained tails present in Main and Gray Phase deposits (Figures 7 and 9) are largely absent in Lithic Phase fall deposits. Sample locations and component legend are shown in Figures 1 and 6, respectively.

Table 4. Vesicle aspect ratios and sizes as calculated from BSE images of pumices KSU-23H (white) and KSU-23A (Gray). Aspect ratios, $a{:}b$, are defined as the ratio of long to short axis, and are calculated from an average of N vesicles for each pumice. Vesicle volumes are calculated by treating the vesicles as oblate spheroids, Vo, spheres, Vs, and prolate spheroids, Vp.

Sample	N	a:b	Vo($10^4 \mu m^3$)	Vs($10^4 \mu m^3$)	Vp($10^4 \mu m^3$)
KSU-23H	36	2.7	6.5	9.6	8.0
	20	2.0	2.3	3.7	1.2
	39	3.2	18.8	33.7	11.5
	16	2.5	5.1	8.1	2.6
	39	3.1	19.0	33.4	12.5
	39	2.8	20.4	34.4	12.8
	22	2.9	9.2	15.7	5.3
	42	4.1	12.8	2.6	13.0
	52	3.2	29.8	53.3	21.9
KSU-23A	34	2.1	3.7	5.4	2.3
	19	2.2	2.5	3.7	1.5
	19	1.9	0.5	0.8	0.2
	12	3.9	0.9	1.7	0.6
	34	3.5	25.0	46.7	22.6
	34	1.4	8.7	10.4	2.5
	22	1.9	4.0	5.6	3.0
	26	1.5	8.7	10.8	3.1
	9	1.6	4.2	5.2	2.1

those in gray pumice; significantly, highly elongate vesicles with aspect ratios greater than 25:1 and "woody" or fibrous textures are common in white pumice (Figure 10), but are absent from gray pumice. White and gray pumice also differ in microlite contents. White pumice contain <1000/mm^3 plagioclase or pyroxene microlites and 0–1000/mm^3 Fe-Ti oxide microlites. Gray pumice contain ~1000/mm^3 plagioclase and pyroxene, and ~10,000/mm^3 Fe-Ti oxide microlites (Figure 11, Table 5).

4. INTERPRETATION AND DISCUSSION

4.1 Eruption Dynamics

Maximum lithic isopleths from pumice fall deposits are shown in Figure 5. Column heights have been calculated from isopleth shapes using the method of Carey and Sparks (1986). Buoyant mass fluxes have been estimated from column heights, using the model of Sparks (1986) and assuming a temperature of 900°C (Izbekov et al., 2003). A range in column height and mass flux is estimated based upon maximum and minimum possible extents for individual isopleths (Table 6). Because each phase erupted both buoyant plumes and pyroclastic flows, we estimate the average total mass fluxes for each eruption phase by dividing the total mass erupted

during that phase by the duration of the phase. Durations of were estimated by dividing the mass of the fall deposits by the mass flux of the buoyant column.

Variations in column height and mass flux versus cumulative volume erupted are displayed in Figure 12. The eruption began with a small phreatomagmatic explosion (Braitseva et al., 1996), but then quickly evolved into a magmatic, Plinian eruption with a column 25–30 km tall, corresponding to a mass flux of 5–10x10^7 kg/s. During the Initial Phase ~1.6 km^3 of magma was deposited as falls and less than 0.25 km^3 as ash. Nearly 6 km^3 of magma and ~1.5 km^3 of lithics was erupted during the Main Phase. Two thirds of that volume was deposited from a buoyant plume 30–36 km tall, with 2.4 km^3 of magma was deposited by pyroclastic flows. Total mass flux during this period was 2–6x10^8 kg/s. Although the Lithic Phase has the smallest volume, 0.26 km^3 of magma and 0.6 km^3 lithics, column height exceeded and intensity of eruption nearly equaled that of the Main Phase (Figure 12). During the Gray Phase, mass flux remained comparable to that of the Lithic Phase, but column height decreased to that of the Initial Phase of eruption (Figure 12). Unlike the preceding eruption intervals, more Gray Phase material was deposited by pyroclastic flows and co-ignimbrite ash falls, 2 km^3 magma and 1.5 km^3 lithics, than from a buoyant plume, 0.8 km^3 magma and <0.1 km^3 lithics. We believe that the increased partitioning of material into non-buoyant pyroclastic flows resulted in less material being present in the buoyant plume, producing an effective decrease in the buoyant mass flux, and thus the plume did not rise as high as during the Main and Lithic Phases.

4.2 Simultaneous Generation of Plumes and Flows

Layers with polymodal size distributions may be products of deposition from mixed sources (e.g., pumice fall and co-ignimbrite ash) or from aggregation of fine-grained material into larger particles (Brazier et al., 1983; Carey and Sigurdsson, 1983). In deposits with accretionary lapilli (e.g. KSU-12E), the origin of bimodal size distributions is apparent. In deposits lacking such salient features, the origin of polymodal size distributions is constrained by stratigraphic relations. For example, sample KSU-01D is a bimodal layer in which most pumice is coated with fine ash, with a prominent 3.5 mm mode and a minor <0.05 mm mode (Table 1,

Table 5. Volumetric number densities of oxide and plagioclase microlites are given for white and Gray pumice. Number densities are reported as microlites per mm^3.

Sample	Plag	Oxide
White	0	800–1300
Gray	0–1000	9800–10500
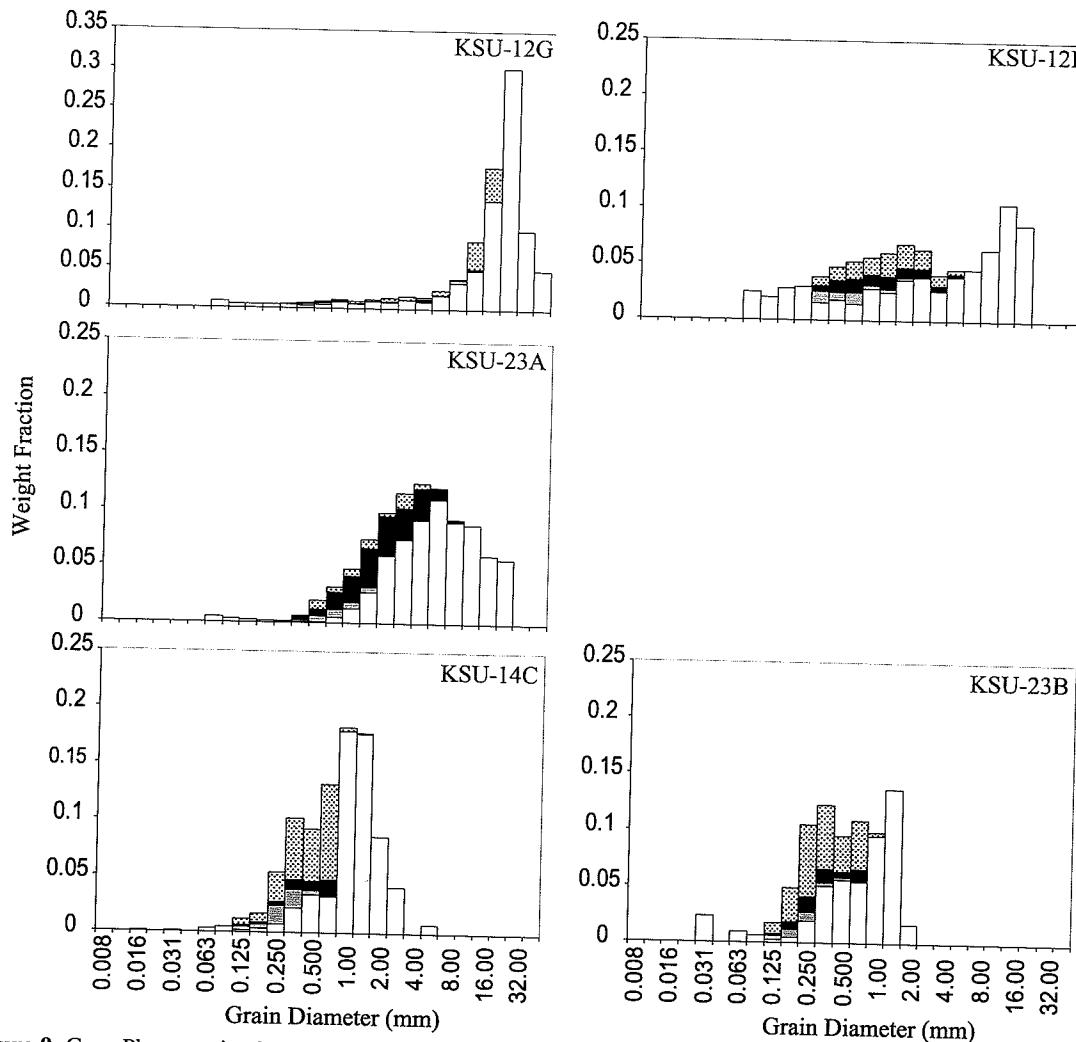
Figure 9. Gray Phase grain size distributions and componentry. Gray phase fall deposits are generally well sorted, though, as with those of the Main phase, they often have fine grained tails. The overlying pyroclastic flow (KSU-12I) and ash (KSU-14B) deposits display polymodal grain size distributions, with medium-grained modes comprised of dense, normal distributed particles. See Figures 1 and 6 for sample locations and component legend.

Figure 7). This layer correlates stratigraphically to pyroclastic flow layers at more proximal sites, and so it is likely KSU-01D is a mixed deposit formed by simultaneous deposition of pumice and ash falls from two plumes, one Plinian and one coignimbrite (Criswell, 1987; Carey et al., 1990; Wilson and Hildreth, 1997; Wilson and Hildreth, 1998).

The following proximal stratigraphic relationships suggest that pyroclastic flows were emplaced over certain sectors of the volcano, while at the same time pumice-fall layers were being deposited over other sectors. Proximal areas have highly variable sequences of interbedded falls and flows (Figure 3b). Those fall layers are not traceable across areas where flow deposits are present. Instead, individual layers are only traceable where pyroclastic flow

deposits are absent. Main and Gray Phase fall layers are not graded above and below flow or ash layers. Instead, those layers are bi-modal and appear to be enriched in fine-grained ash. The coarse modes of pumice-rich ashes are similar *to* those of Plinian falls. These relationships

Table 6. Column heights and mass discharge rates (MDR) as calculated using the methods of Carey and Sparks (1986) and Sparks (1986). Three to four isopleths were averaged for each phase

| Phase	Height (km)	MDR (kg/s)
Initial	25–30	$5–10 \times 10^7$
Main	30–36	$2–6 \times 10^8$
Lithic	30–37	$1–4 \times 10^8$
Gray	27–30	$2–3 \times 10^8$
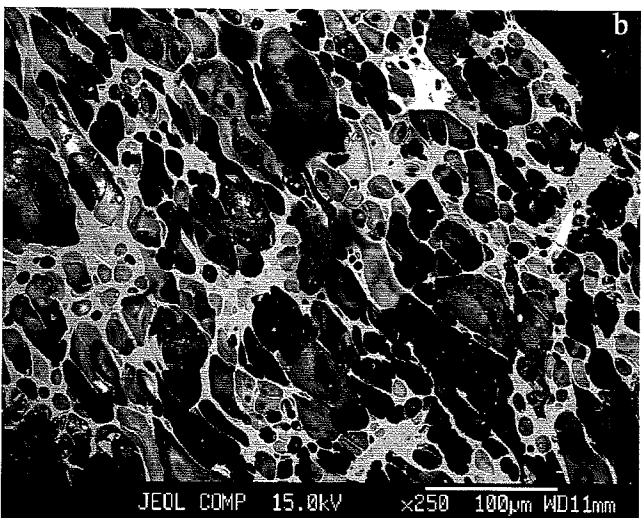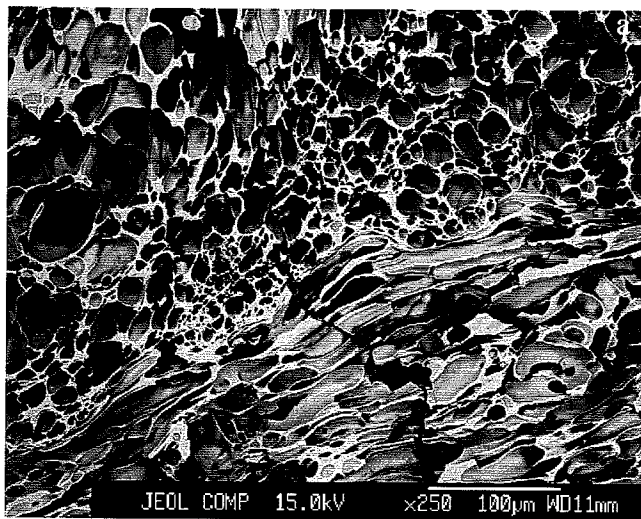
Figure 10. BSE images of a) white and b) gray pumice illustrating differences in vesicle shape and distribution. Note that white pumice contain larger, more elongate vesicles than gray pumice. Vesicle aspect ratios in white pumice can be greater than 20, whereas in gray pumice the vesicles are generally more equant (Table 4).

indicate that tephra was simultaneously deposited from vent-sourced and co-ignimbrite plumes.

Similar behavior (e.g., simultaneous eruption of a buoyant plume and non-buoyant flows) was observed during the 1980 Mount St. Helens (Criswell, 1987) and 1991 Pinatubo eruptions (Paladio-Melosantos et al., 1996), and is suggested to have occurred during the 79 A.D. Vesuvius eruption (Carey and Sigurdsson, 1987) and 1912 Katmai-Novarupta eruption (Houghton et al., 2004). Column instability manifests itself when insufficient air is entrained for the column to become buoyant, at which point the column partially or completely collapses and non-buoyant pyroclastic flows are shed. When

instability begins, discrete flows are generated, at least initially, over certain sectors of the volcano (e.g., Neri et al. 2002; Kaminski et al., 2005), rather than the entire column collapsing and depositing material on all flanks of the mountain. Numerical and analog studies by Wilson et al. (1980), Dobran et al. (1993), and Neri et al. (2002) predict column instability when mass flux typically exceeds 10^8 kg/s. Interestingly, the Plinian column of the KS_1 eruption became unstable when mass flux exceeded 10^8 kg/s.

Unlike earlier eruption phases, the Gray Phase erupted a greater volume as pyroclastic flows than as a buoyant column. In addition, the relative proportion of fine ash in bimodal fall samples is greater in Gray Phase samples than in samples from
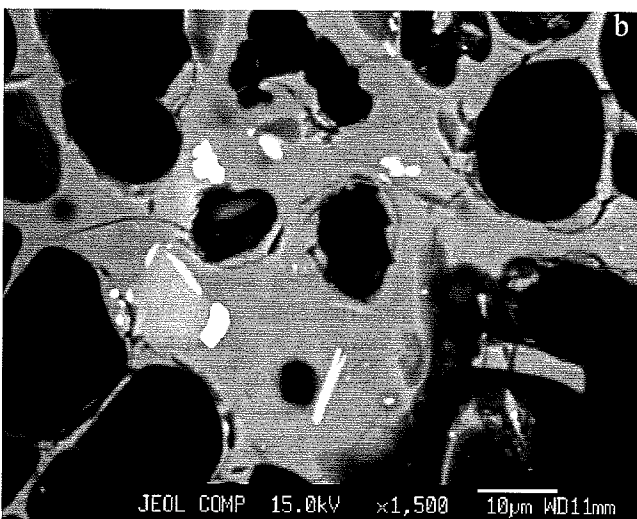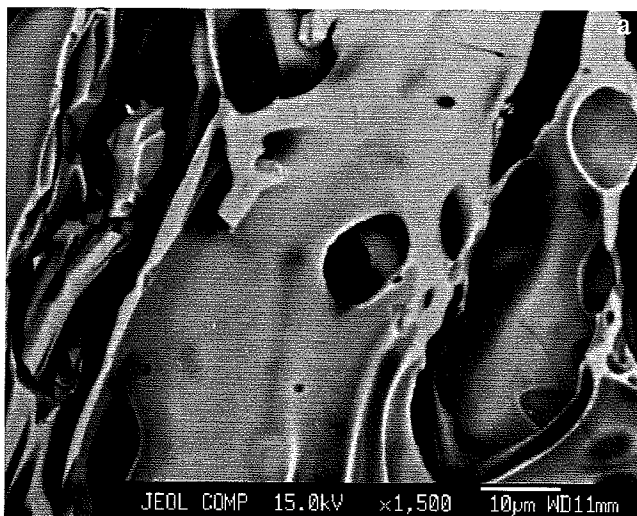
Figure 11. BSE images of a) white and b) gray pumice illustrating differences in microlite content. Note that Fe-Ti oxide, plagioclase, and pyroxene microlites are present in gray pumice but not present in white (Table 5).
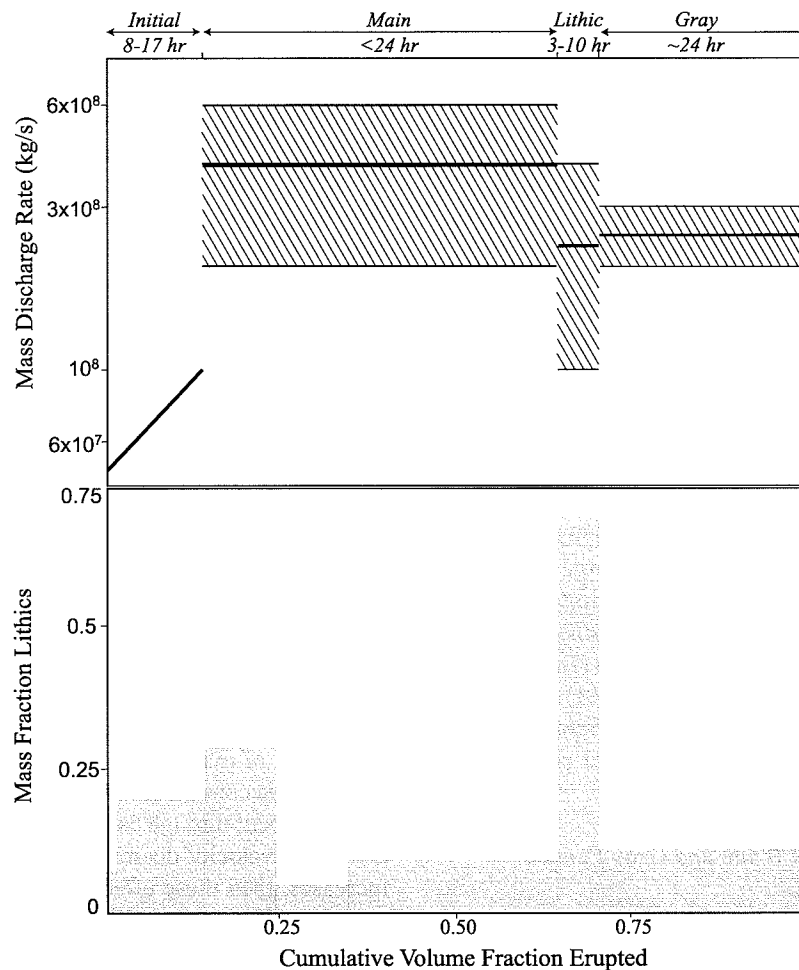
Figure 12. Eruption timeline. Average mass flux is indicated by the bold line and diagonal-hatched regions; the mass fraction of lithic clasts erupted is shown by the gray regions. The approximate durations and volume erupted during each phase of eruption are indicated at the top and bottom, respectively, of the figure.

other phases. That greater relative proportion of fine ash probably reflects a greater proportion of co-ignimbrite ash to Plinian ash fall. These observations suggest that a higher proportion of pyroclastic flows were generated during the Gray Phase than in earlier phases (Figures 6–9) even though mass flux was lower than during the Main Phase (Figure 12). Given the fact that the white and gray pumice were both derived from essentially identical magma, in principle the reverse correlation might be expected. This may indicate a strong dependence of column behavior on vent geometry, and hence that a rapid change in geometry may have taken place (i.e. caldera collapse) preceding eruption of the Gray Phase (Wilson et al., 1980).

4.3 Timing of Caldera Formation

Braitseva et al. (1996) and others have argued conclusively that Caldera V formed during the KS_1 eruption, but one question

that remains is when did the caldera collapse during this eruption? Throughout the Initial, Main, and most of the Gray Phases, lithics constitute ~25 wt.% or less of the deposits. During the Lithic Phase, however, lithics account for greater than 50 wt.% of the deposits. Although the total volume of lithics in Lithic Phase deposits is less than that of either the Main or Gray Phases, the rate at which they were erupted is substantially greater. Given estimates for mass fluxes for the different phases, lithic ejection rates for the Lithic Phase are up to 1.4×10^8 kg/s, whereas those of the Main and Gray phases are $\sim 4.3 \times 10^7$ kg/s. It is unlikely this represents solely rapid widening of a central vent, because that would have led to a substantial increase in mass flux (Wilson et al., 1980; Woods, 1988), which is not observed (Figure 12). Instead, we propose that the large increase in lithics resulted from collapse of the caldera during the Lithic Phase and continued into the beginning of the Gray Phase, given that its lowest deposit has up to 40 wt% lithics.

Assuming that caldera collapse occurred during the Lithic phase of the eruption, then it formed after ~66% of the volume had been erupted. Interestingly, the amount of magma erupted prior to the Lithic phase, ~7 km^3, is equal to the collapse volume estimated by Braitseva et al. (1996). This contrasts with observations of typical caldera formation (e.g., Bacon, 1983), in which the majority of volume is inferred to have erupted after caldera collapse. Gardner and Tait (2000) noted a similar relation between erupted volume and collapse timing at Volcán Ceboruco, where approximately ~75% of the magma erupted prior to caldera formation. Changes in mass flux during the KS$_1$ producing eruption are also similar to those of the caldera-forming eruption of Volcán Ceboruco in which mass flux decreased during the initiation of collapse (Gardner and Tait, 2000). Gardner and Tait (2000) suggest that a critical volume of magma must be erupted prior to caldera collapse, and that there may be some fundamental difference in the mechanics of large and small caldera collapses; large calderas seem to begin to collapse early (volumetrically) in the eruption, whereas small calderas may initiate near the conclusion of the eruption (Browne and Gardner, 2004). Indeed, Roche and Druitt (2001) describe a set of collapse criteria that predict early, coherent, "piston" collapse of large calderas and late piecemeal collapse of small calderas.

4.4 The Difference Between White and Gray Pumice

Collapse of Caldera V seems to correspond to the change in pumice texture, from white to gray pumice. The abrupt change in pumice color occurring in the KS$_1$ deposit seems to mark a correlatable time horizon. Similar abrupt changes in pumice color during caldera-forming eruptions are not uncommon and usually reflect a substantial change in composition, such as those of the 1912 Katmai, 7.7 k.a. eruptions Crater Lake (e.g., Hildreth, 1983; Bacon and Druitt, 1988). In contrast, the bulk compositions of the Ksudach pumice are the same: rhyodacitic 71.5–72 wt.% SiO$_2$ (Volynets et al., 1999; Izbekov et al., 2003). Moreover, magnetite-ilmenite geothermometry indicates that the magma(s) that formed the white and gray pumice equilibrated at similar temperatures, ~892 +/-7 °C and oxygen fugacities of -11.5 +/-0.2 (log f_{O2}), respectively (Izbekov et al., 2003). Both pumice types have the same phenocryst assemblage (plagioclase, orthopyroxene, clinopyroxene, magnetite and ilmenite) and consist of greater than 90% glass. Thus a single magma body was tapped throughout the KS$_1$ eruption.

White and gray pumice differ markedly in microlite populations and vesicle textures, despite their identical compositions (Tables 4 and 5). That change in texture may record the transformation of the conduit and vent structure. The elongated vesicles (Table 4) in white pumice could result from a higher strain rate from greater shear (Manga et al., 1998). If so, then this would argue for slower ascent velocity of the gray magma, because the mass flux of the Gray Phase is similar to that of the Main and Lithic Phases (Figure 12).

Support for slower decompression is found in the differences in microlite content between the white and gray pumice (Table 5). Plagioclase and pyroxene microlites are present in number densities of ~1000 mm^{-3} in gray pumice and <1000 mm^{-3} in white. Because time is required for crystals to nucleate and grow (Geschwind and Rutherford, 1995,; Hammer and Rutherford, 2002; Couch, 2003), the marked increase in plagioclase, pyroxene, and Fe-Ti microlites in the gray pumice suggest that the gray magma decompressed more slowly.

Interestingly, the mass flux of the Gray phase is similar to that of the Main and Lithic phases and greater than that of the Initial phase (Table 6), yet pumice appear to record two different ascent rates, with gray pumice ascending slower than white ones. Given that mass flux was similar between Lithic and Gray phases, the change in velocity may suggest that the conduit cross-sectional area increased a change that could be consistent with caldera collapse. Lastly, the higher proportion of pyroclastic flows generated during the Gray phase is also consistent with a change in vent geometry, such as might occur through caldera collapse. All else being equal, if the exit velocity decreases while the area of the conduit increases, then these effects should both combine to make column collapse more likely, and hence lead to a greater proportion of pyroclastic flows.

5. CONCLUSION

Field and stratigraphic observations indicate that the KS$_1$ eruption progressed in four distinct phases of eruption: Initial, Main, Lithic, and Gray. Granulometric and component analyses suggest fall deposition by both vent sourced and co-ignimbrite plumes. Mass flux varied during the eruption by as much as an order of magnitude, from 5–10x10^7 kg/s during the Initial Phase, to a maximum of 2–6x10^8 kg/s in the Main Phase. Mass flux during the Lithic Phase dropped by as much as a factor of 3, before increasing during the Gray Phase to 2–3x10^8 kg/s. When mass flux exceeded 10^8 kg/s, buoyant plumes and non-buoyant pyroclastic flows were simultaneously erupted. Caldera collapse is probably marked by the major influx of lithics during the Lithic Phase. Collapse thus occurred after eruption of ~6.1 of the 8.5 km^3 of magma (DRE) erupted. Changes in conduit and column dynamics were heralded by collapse, leading to slower magma ascent, marked by the white-gray pumice transition, and increased generation of pyroclastic flows.

REFERENCES

Bacon, CR, 1983. Climactic eruption of Mount Mazama and formation of Crater Lake caldera, Oregon. United States Geological Survey Professional Paper: 141–142.

Bacon, CR and TH Druit, 1988. Compositional evolution of the zoned calcalkaline magma chamber of Mount Mazama, Crater Lake, Oregon. Contributions to Mineralogy and Petrology, 98: 224–256.

Braitseva, OA, IV Melekestsev, VV Ponomareva, and VY Kirianov, 1996. The caldera-forming eruption of Ksudach volcano about cal. A.D> 240: the greatest explosive event of our era in Kamchatka, Russia. Journal of Volcanology and Geothermal Research, 70: 49–65.

Brazier, S, RSJ Sparks, SN Carey, H Sigurdsson, and JA Westgate, 1983. Bimodal grain size distribution and secondary thickening in air-fall ash layers. Nature, 301: 115–119.

Browne, B, and JE Gardner, 2004. The nature and timing of caldera collapse as indicated by accidental lithic fragments from the ~1000 A.D. eruption of Volcán Ceboruco, Mexico. Journal of Volcanology and Geothermal Research, 130: 93–105.

Bursik, M, IV Melekestsev, and OA Braitseva, 1993. Most recent fall deposits of Ksudach Volcano, Kamchatka, Russia. Geophysical Research Letters, 20: 1815–1818.

Carey, SN, and H Sigurdsson, 1983. Influence of particle aggregation on deposition of distal tephra from the May 18, 1980, eruption of Mount St. Helens volcano. Journal of Geoyphysical Review, 87: 7061–7072.

Carey, S and RSJ Sparks, 1986. Quantitative models of the fallout and dispersal of tephra from volcanic eruption columns. Bulletin of Volcanology, 48: 109–125.

Carey, S and H Sigurdsson, 1987. Temporal variations in column height and magma discharge rate during the 79 A.D. eruption of Vesuvius. Geological Society of America Bulletin, 99: 303–314.

Carey, S, H Sigurdsson, JE Gardner, and W Criswell, 1990. Variations in column height and magma discharge during the May 18, 1980 eruption of Mount St. Helens. Journal of Volcanology and Geothermal Research, 43: 99–112.

Cioni, R, R Sulpizio, and N Garruccio, 2003. Variability of the eruption dynamics during a subplinian event; the Greenish Pumice eruption of Somma-Vesuvius (Italy). Journal of Volcanology and Geothermal Research, 124: 89–114.

Couch, S, 2003. Experimental investigation of crystallization kinetics in a haplogranite system. American Mineralogist, 88: 1471–1485.

Criswell, CW, 1987. Chronology and pyroclastic stratigraphy of the May 18, 1980 eruption of Mount St. Helens, Washington. Journal of Geophysical Research, B, 92: 10237–10,266.

Dobran, F, A Neri, and G Macedonio, 1993. Numerical simulations of collapsing volcanic columns. Journal of Geophysical Research, B, 98: 4231–4259.

Fierstein, JE and M Nathenson, 1992. Another look at the calculation of fallout tephra volumes. Bulletin of Volcanology, 54: 156–167.

Gardner, JE, RME Thomas, C Jaupart, and S Tait, 1996. Fragmentation of magma during Plinian volcanic eruptions. Bulletin of Volcanology, 58: 144–162.

Gardner, JE, and S Tait, 2000. The caldera-forming eruption of Volcán Ceboruco, Mexico. Bulletin of Volcanology, 62: 20–33.

Geschwind, C-H and MJ Rutherford, 1995. Crystallization of microlites during magma ascent: the fluid mechanics of the 1980–1986 eruptions at Mount St. Helens. Bulletin of Volcanology, 57: 356–370.

Hammer, JE, KV Cashman, RP Hoblitt, and S Newman, 1999. Degassing and microlite crystallization during the pre-climactic events of the 1991 eruption of Mt. Pinatubo, Philippines. Bulletin of Volcanology, 60, 355–380.

Hammer, JE and MJ Rutherford, 2002. An experimental study of the kinetics of decompression-induced crystallization in silicic melt. Journal of Geophysical Research, B, 107.

Hildreth, W, 1983. The compositionally zoned eruption of 1912 in the Valley of Ten Thousand Smokes, Katmai National Park, Alaska. Journal of Volcanology and Geothermal Research, 18: 1–56.

Houghton, BF, CJN Wilson, J Fierstein, and W Hildreth, , 2004. Complex proximal deposition during the Plinian eruptions of 1912 at Novarupta, Alaska. Bulletin of Volcanology, 66: 95–133.

Izbekov, P, JE Gardner, B Andrews, VV Ponomareva, and IV Melekestsev, 2003. Petrology of Holocene caldera-forming eruptions at Ksudach, Kamchatka. EOS Transactions AGU, 84(46), Fall Meeting Supplement, Abstract V42B-0347.

Kaminski, E, S Tait, and G Carazzo, 2005. Turbulent entrainment in jets with arbitrary buoyancy. Journal of Fluid Mechanics, 526: 361–376.

Manga, M, J Castro, KV Cashman, and M Loewenberg, 1998. Rheology of bubble-bearing magmas. Journal of Volcanology and Geothermal Research, 87: 15–28.

Neri, A, A DiMuro, and M Rosi, 2002. Mass partition during collapsing and transitional columns by using numerical simulations. Journal of Volcanology and Geothermal Research, 115: 1–18.

Paladio-Melosantos, MLO, RU Solidum, WB Scott, RB Quiambao, JV Umbal, KS Rodolfo, BS Tubianoso, PJ de los Reyes, RA Alonso, and HB Ruelo, 1996. Tephra falls of the 1991 eruptions of Mount Pinatubo. In: Fire and Mud: 512–535.

Pyle, DM, 1989. The thickness, volume, and grain-size of tephra fall deposits. Bulletin of Volcanology, 51: 1–15.

Roche, O and TH Druitt, 2001. Onset of caldera collapse during ignimbrite eruptions. Earth and Planetary Science Letters, 191: 191–202.

Sparks, RSJ, 1986. The dimensions and dynamics of volcanic eruption columns. Bulletin of Volcanology, 48: 3–15.

Volynets, ON, VV Ponomareva, OA Braitseva, IV Melekestsev, and ChH Chen, 1999. Holocene eruptive history of Ksudach volcanic massif, South Kamchatka: evolution of a large magmatic chamber. Journal of Volcanology and Geothermal Research, 91: 23–42.

Walker, GPL, 1981. Plinian eruptions and their products. Bulletin of Volcanology, 44: 223–240.

Wilson, L, RSJ Sparks, and GPL Walker, 1980. Explosive volcanic eruptions, IV, The control of magma properties and conduit geometry on eruption column behavior. Geophysical Journal of the Royal Astronomical Society, 63, 117–148.

Wilson, CJN, and WH Hildreth, 1997. The Bishop Tuff: new insights from eruptive stratigraphy. Journal of Geology, 105: 407–439.

Wilson, CJN, and WH Hildreth, 1998. Hybrid fall deposits in the Bishop Tuff, California; a novel pyroclastic depositional mechanism. Geology, 26: 7–10.

Woods, AW, 1988. The fluid dynamics and thermodynamics of eruption columns. Bulletin of Volcanology, 50: 169–193.

Benjamin J. Andrews, Department of Geology and Geophysics, Jackson School of Geosciences, The University of Texas at Austin, 1 University Station C1100, Austin, TX 78712-0254, email: andrewsb@mail.utexas.edu